RESEARCH ARTICLE | MARCH 18 2026

Experimental investigation of the vortex ring state for side-by-side propellers in descent flight

G. Bucherelli ; D. Granata ; A. Savino ; A. Zanotti

Physics of Fluids 38, 035136 (2026)
https://doi.org/10.1063/5.0311688

Physics of Fluids ARTICLE pubs.aip.org/aip/pof

Experimental investigation of the vortex ring state for side-by-side propellers in descent flight

Cite as: Phys. Fluids **38**, 035136 (2026); doi: 10.1063/5.0311688
Submitted: 11 November 2025 · Accepted: 5 March 2026 ·
Published Online: 18 March 2026

G. Bucherelli, D. Granata, A. Savino, and A. Zanotti[a)]

AFFILIATIONS

Politecnico di Milano, Dipartimento di Scienze e Tecnologie Aerospaziali, via La Masa 34, 20156 Milan, Italy

[a)]Author to whom correspondence should be addressed: alex.zanotti@polimi.it

ABSTRACT

The present paper describes an experimental wind tunnel campaign aimed at investigating the aerodynamic interactions between two side-by-side (SBS) propeller models operating in Vortex Ring State (VRS) conditions. Load measurements and Particle Image Velocimetry (PIV) were employed in this comprehensive test campaign. Several configurations were considered, varying the tip-to-tip distance between the SBS propellers (i.e., with aligned propeller disks) in both co-rotating and counter-rotating configurations. The test results enabled characterization of the mutual aerodynamic influence between the two SBS propellers, providing insight into the loss of performance that occurs when the propellers enter this specific descent flight condition. Moreover, PIV measurements provided a detailed characterization of the velocity flow field and the dimensions of the vortical structures associated with VRS occurrence across the different configurations tested.

I. INTRODUCTION

One of the most critical aerodynamic conditions concerning safety for rotorcraft is the Vortex Ring State (VRS), which occurs during the vertical descent phase of a rotor or propeller, particularly when the descent rate becomes comparable to the induced velocity of the rotor at the rotor plane.[1,2] In this flight condition, the rotor or propeller descends into its own wake, causing the airflow to recirculate around the rotor disk in the form of an annular vortex. This leads to a significant loss of thrust, generally resulting in reduced control, stability, and performance.[3] This phenomenon has been extensively investigated for rotors, particularly with application to helicopters or tilt-rotors.[4–7] The complexity in flow topology that characterizes the VRS phenomenon renders low-order methods based on momentum theory inapplicable, as a well-defined slipstream through the rotor disk is no longer present. As a result, flight tests and wind tunnel experiments become essential for understanding and predicting the physics of VRS.[8]

Many experimental studies available in the literature have focused on investigating a single propeller in the descent phase in order to identify both the most critical flight parameters, such as descent rate and angle, and the effect of the propeller design.[6,7] The experimental study by Betzina[4] investigated VRS on a scaled rotor-wing configuration of the Bell–Boeing V-22 Osprey, testifying severe low-frequency roll oscillations and thrust fluctuations with the same frequency, in addition to the thrust reduction typical of the phenomenon onset. The same tilt-rotor configuration is analyzed in the work by Brand *et al.*,[5] where an operational envelope for the aircraft is defined and flight regimes free from the vortex ring state are demonstrated.

Although the phenomenon of the vortex ring state has been extensively studied in conventional single-rotor configurations, as highlighted by Brown,[9] the development of new rotorcraft configurations for Urban Air Mobility (UAM) applications introduces new challenges. The latest developments in the aerospace industry have led to a strong focus on Electric Vertical Take-Off and Landing (eVTOL) aircraft, which are characterized by electric propulsion, tilt-wing configurations, and multiple rotors. This last aspect represents a challenge as the consequent aerodynamic interaction significantly affects aerodynamic performance, efficiency, and noise generation, making its study essential for the successful implementation of UAM solutions. Aerodynamic interactions, together with other distinctive eVTOL characteristics, such as rotational speed control, lift generation from wings, and thrust vectoring, justify a revaluation of VRS susceptibility with respect to conventional rotorcraft. In addition, the combination of compact geometries and relatively low weight broadens the flight envelope in which VRS may occur for this kind of aircraft, and the presence of small rotors, high blade twist, and lateral rotor arrangements increases sensitivity to VRS. To address these differences, some studies have investigated the VRS behavior in eVTOL configurations

employing different methods. A recent contribution by Jeong *et al.*[10] exemplifies this effort. In this work, a helicopter-based engineering model was extended to capture the effects of blade geometry and descent trajectories on VRS onset in eVTOLs. This adapted model allows for the comparison of VRS susceptibility across different aircraft configurations and flight profiles. In particular, the obtained results suggest that the relatively low aerodynamic drag found in certain eVTOL configurations may increase susceptibility to VRS. This reinforces the need for further investigation into how eVTOL design features influence VRS onset and progression.

The study by Veismann *et al.*[2] presented a parametric analysis to provide an experimental assessment of the influence of relevant rotor blade design parameters on the descent performance of a small-scale rotor. The choice of better adapting a rotor for descent scenarios is not driven by efficiency considerations but much more by safety concerns, since descent is typically considered the most hazardous flight stage. In fact, solely focusing the design process on hover conditions and disregarding any descent considerations may cause future rotor designs to lead toward unstable descent performance, where even operational measures cease to be effective. The investigation conducted by Pickles *et al.*[11] showed that shrouded rotors enter the VRS similarly to their isolated counterparts, and the presence of the shroud may be responsible for a slight delay of its onset. A very recent contribution to the study of VRS for a real eVTOL propeller geometry is provided by Savino *et al.*[12,13] describing results of a collaboration between Politecnico di Milano (POLIMI) and Archer Aviation aimed at investigating through wind tunnel tests the occurrence and correlated flow physics of this phenomenon applied to the scaled geometry of the Archer Maker tilter propeller.

Despite increasing attention to this issue, the literature still lacks comprehensive and structured studies directly addressing VRS in multirotor configurations, resembling a more realistic configuration for an eVTOL aircraft, and mainly limited to flow field evaluations.[14] However, the growing body of research on rotor–rotor aerodynamic interactions[15–17] reflects the increasing recognition of its relevance and urgency. Among the various aerodynamic phenomena affecting eVTOL performance, rotor–rotor interactions play a central role, especially due to the typical multirotor configurations used in these vehicles, where close spacing between propellers makes aerodynamic interference inevitable. As this type of aircraft often features multiple propellers placed close together, the side-by-side (SBS) configuration is a typical example. Due to the potential for aerodynamic interference, this setup has gained increasing attention in recent research. When propellers are closely spaced, they can experience significant wake interactions, which may lead to performance loss, unsteady aerodynamic loads, and even early onset of VRS. These challenges highlight the need for focused studies on rotor interactions in eVTOL designs.

The study by Longobardo *et al.*[8] has recently addressed this scientific quest by investigating and comparing the Vortex Ring State for an isolated propeller and a quadrotor configuration, which constitutes a promising design among the eVTOL ones already extensively discussed in the literature. Thrust and power measurements, as well as Stereo Particle Image Velocimetry (S-PIV) covering the whole area of flight susceptible to VRS, showed the quadrotor configuration to be more affected by this phenomenon with respect to the isolated propeller case. In particular, although the mean thrust reduction was similar when comparing the two configurations, the quadrotor configuration demonstrated a broader region of the flight envelope characterized by significant mean thrust reduction when compared to the isolated rotor configuration, with the onset, development, and decrease in the VRS occurring earlier with respect to descent ratio (DR) and more gradually. Moreover, PIV measurements showed a single recirculation region wrapping around the quad-rotor model at the onset of VRS, with the generation of a unified vortex ring due to the lateral vicinity between the rotors.

The present paper aims at contributing to reduce the gap still present in the literature concerning VRS investigation involving rotor interaction phenomena. The results of an experimental study based on a comprehensive wind tunnel campaign on two side-by-side eVTOL propeller models in VRS conditions are presented and discussed. The present wind tunnel campaign is part of the activities of the recent GARTEUR Action Group RC-28 "eVTOL aircraft Vortex-Ring-State investigations." As a partner of this consortium, Politecnico di Milano (POLIMI) contributed to the activities of this Action Group by providing a comprehensive experimental database over a test case with open geometry suitable for a robust validation of the partners' numerical models with different levels of fidelity. The experimental database included both loads and velocimetry results. Load measurements were used to quantify aerodynamic performance variation with respect to hover under descent flight conditions, while Particle Image Velocimetry (PIV) was aimed to investigate the flow physics around the dual-propellers system area. In particular, in order to characterize the VRS phenomenon for architectures typical of eVTOL aircraft, wind tunnel tests included an isolated propeller case, to be considered as a reference, and multiple side-by-side configurations with aligned propeller disks and different lateral distance between the propellers. Moreover, the effect of the blades' sense of rotation was also investigated by comparing test results with both co-rotating and counter-rotating propellers. The aim of the tests was to characterize the mutual aerodynamic influence between the two side-by-side propellers, providing insight into the loss of performance occurring on the propellers when entering the VRS condition. Comparing the different side-by-side configurations also allows one to identify the design choices that would be convenient in terms of VRS occurrence. Moreover, flow field surveys were performed to get a detailed characterization of the velocity field and the vortical structures associated with the VRS phenomenon in the different configurations tested, as well as propeller wakes' interactions. Finally, the comprehensive test campaign was aimed at collecting an experimental database to be used to provide guidelines for an effective and safe design of novel eVTOL architectures.

II. EXPERIMENTAL SETUP

The experimental campaign was conducted in the Sergio De Ponte wind tunnel of the Department of Aerospace Science and Technology (DAER) of Politecnico di Milano, a closed-loop facility located at the Aerodynamics Laboratory of the Department. The facility features a $1.5 \times 1\ m^2$ test section and can reach a maximum velocity of 58 m/s with a turbulence level below 0.1%. The experimental setup was characterized by two scaled propeller models[16] equipped with three-bladed VarioProp 12C propellers, each with a nominal diameter of 300 mm.[16] The propeller setup in the test section of the wind tunnel is shown in Fig. 1. The blades, made of a hobby-grade composite material, are attached to a central hub that allows for the simultaneous adjustment of their collective pitch angle. Each hub is coupled with a 65 mm diameter aluminum spinner, designed to streamline the airflow

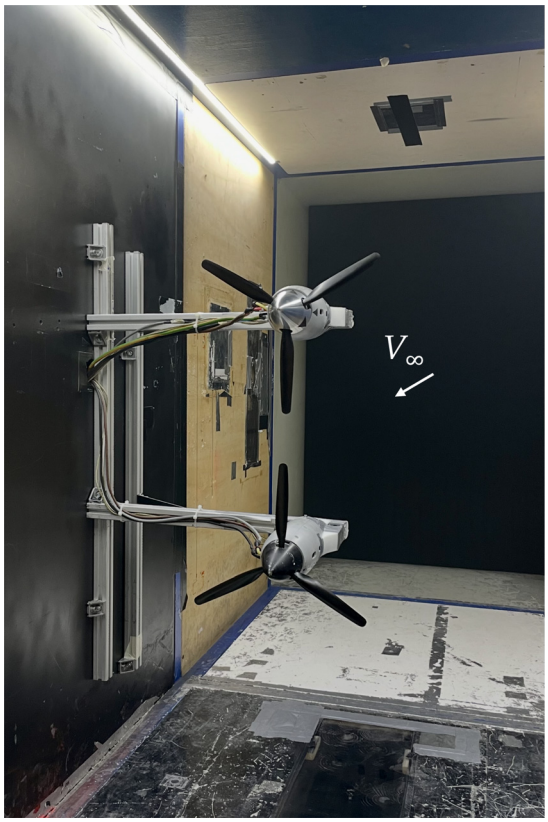

FIG. 1. Layout of the VRS side-by-side propellers experimental setup at S. De Ponte wind tunnel of Politecnico di Milano.

around the root region and minimize undesired aerodynamic disturbances in the hub zone. The propeller system is driven by a Scorpion HKII-4235-630 kV brushless electric motor, offering a continuous power output of 5.3 kW. The motor is powered and regulated through a PWM-controlled ESC (Scorpion Tribunus II 06-120A SBEC). The rotor hubs are equipped with a Hall-effect sensor positioned beneath the motor assembly to provide one signal per revolution for rotational speed monitoring. Rotational speed is regulated using a custom LabVIEW-based control system, which also handles data acquisition. The RPM control system allowed a maximum error of 1% of the target rotational speed of the two propellers. Due to hardware limitations in the available hobby-grade ESC system, the blade azimuth phase of the propellers was not synchronized. However, the phase offset was considered negligible for the objectives of the experimental campaign. The motor, hub, and instrumentation of each propeller are housed within a custom-made polycarbonate nacelle of 270 mm length, manufactured using Fused Deposition Modeling (FDM) 3D printing. An internal aluminum support frame ensures rigid mounting and correct load transmission to a bi-axial strain gauge balance, allowing for accurate aerodynamic force measurements.

The propeller configuration was tailored to reproduce descent flight conditions. Therefore, the propellers were mounted so that the wind tunnel flow impinged on them from below, simulating the relative flow direction during vertical descent. The propellers were

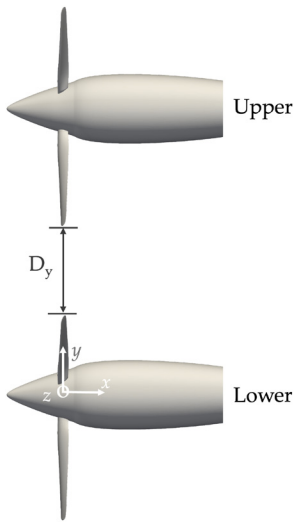

FIG. 2. Layout of the propeller models with orthogonal axes.

mounted vertically aligned on a metallic frame constructed from Bosch aluminum profiles. This frame was designed to allow vertical translation of one propeller, enabling precise control of the tip-to-tip distance during the test campaign. To minimize wall interference effects, the entire assembly was centered within the test chamber. Given the upward-facing flow, dedicated fairings were designed and 3D-printed to streamline exposed surfaces and reduce flow separation. These fairings smoothed the transition between the nacelle and its support arm, while a beveled leading edge was added to the support bar to reduce flow disturbances caused by abrupt geometric discontinuities. To measure the aerodynamic loads generated by the propeller, a FUTEK MBA500 bi-axial strain gauge load cell was integrated within the internal structure of the nacelle. This sensor features a full-scale range of ±222.4 N for thrust and ±5.65 N m for torque (non-linearity ±0.25% rated output and non-repeatability ±0.05% rated output). The load cell was embedded within a dedicated housing of the model, with the fixed side rigidly attached to the base support structure and the active side connected to the load transmission interface linked to the propeller hub. A small clearance was maintained to ensure that the cylindrical, non-sensitive part of the sensor did not come into contact with the surrounding polycarbonate nacelle, allowing for free-of-interference operation. The sensor outputs were acquired using a National Instruments CompactDAQ system, equipped with a NI-9237 strain/bridge input module. Data acquisition was performed at a sampling rate of 25 kHz, and for each operating point, four acquisition runs were recorded to ensure the repeatability of the results and reduce the influence of transient effects. The acquired signals were then averaged. The acquisition and control procedures were managed through a custom-developed LabVIEW software environment. This setup allowed for real-time monitoring of both the propeller loads and the wind tunnel parameters, including dynamic pressure, air temperature, and atmospheric pressure. A schematic layout of the two propellers is shown in Fig. 2. The orientation of the reference axes adopted as a convention throughout this work is highlighted in the scheme, as well as the distance between the propellers in the y-direction, D_y, which will be used as the control parameter. In this work, D_y is defined as the

lateral tip-to-tip distance between the propellers along the y-axis and is expressed as a fraction of the propeller radius. The lower propeller is taken as the reference, while the upper propeller is displaced in order to vary the distance D_y to investigate interactional effects.

The test matrix is reported in Table I. For each configuration, the wind tunnel speed was systematically varied, covering descent ratios (DRs) from 0 up to approximately 2, while the rotational speed of both propellers was kept fixed at 7000 RPM. Reynolds number based on blade chord and blade rotational velocity evaluated at 75% of the propeller radius corresponds to $Re_c = 1.16 \times 10^5$. Descent ratio is defined in this work as the ratio between the magnitude of the wind tunnel freestream velocity and the single propeller induced velocity evaluated in hover (v_h). For each test, the wind tunnel freestream velocity was manually adjusted to achieve the range of descent ratio around the VRS onset. During the tests, the collective pitch angle θ of both propeller blades, considered at 75% of the propeller radius (R), was kept fixed at 12°. Given the importance of the hover thrust value, which was used as a reference in performance metrics and comparisons as well as for the definition of DR, an independent, additional measurement campaign was performed on the single propeller outside the wind tunnel test section, allowing the acquisition of unconfined thrust data free from wall interference effects.

Two-dimensional PIV surveys were employed to characterize the flow field generated by the dual-propellers system. The experimental arrangement included a dual-head Nd:YAG Quantel Evergreen laser ($\lambda = 532$ nm, 200 mJ per pulse), positioned beneath the transparent floor of the wind tunnel. A 90° optical mirror was used to redirect the laser beam upward, forming a planar light sheet approximately with the longitudinal plane of the model for flow field illumination. Due to mechanical constraints related to the placement of the calibration target, the light sheet was positioned with a 58 mm offset from the mid-span section of the two propellers. Two ILA.PIV.sCMOS cameras (16-bit, 2560 × 2160 pixels) were installed outside the test section in a vertical tandem configuration. A slight overlap between the camera fields of view enabled the reconstruction of a larger measurement window, allowing the investigation of the flow field area around the two propellers. The cameras were rigidly mounted on an external frame to ensure proper alignment and to minimize vibrations. Flow seeding was performed using a PIVTEC PIVpart30 generator equipped with Laskin nozzles, producing oil-based tracer particles with diameters in the range of 1–2 μm. Figure 3 shows a sketch of the laser setup and a picture of the cameras setup in the test section, including the calibration target. Free-run acquisition of 500 double-frame image pairs was collected for each test configuration. PIV image analysis was performed using PIVview 3C software by PIVTEC GmbH.[18] A multi-pass, multi-grid cross correlation algorithm was applied, with interrogation windows starting from 128 × 128 pixels down to 32 × 32 pixels. This resulted in a resolution between adjacent measurement points of about 3 mm. The accuracy of the PIV measurements was calculated taking into account the pulse-separation time and the optical magnification used for the present tests and considering a maximum displacement error of 0.1 pixels.[19] This leads to a maximum in-plane velocity error below 2% of the maximum in-plane velocity component measured in the investigated flow fields.[20] Regions obscured by the nacelle or propeller blades were masked during post-processing. To effectively characterize the descent condition and investigate the onset and development of VRS, four descent ratios were selected among those considered in the test matrix for each propeller configuration tested. These freestream velocities were selected to span from near-hover conditions to descent regimes with increasing severity, allowing the progressive transition into and out of the VRS to be captured.

TABLE I. Load measurements test matrix.

Configuration	D_y	Rotation sense	DR (-)
Single	...	...	0–2
Side-by-side	1R	Co-rotating	0–2
Side-by-side	0.5R	Co-rotating	0–2
Side-by-side	0.3R	Co-rotating	0–2
Side-by-side	0.1R	Co-rotating	0–2
Side-by-side	0.1R	Counter-rotating	0–2

III. RESULTS AND DISCUSSION

A. Load measurement

For the discussion of thrust measurements regarding the configurations involving the two side-by-side (SBS) propellers, the lower propeller was used as the primary reference, allowing for a consistent comparison of thrust and torque behavior with respect to the isolated propeller configuration. As a matter of fact, the analysis of the loads measured on the upper propeller confirms an analogous behavior in terms of performance due to the identical setup used for the

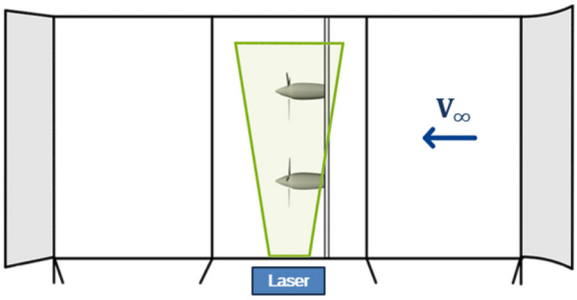

(a)Laser set-up

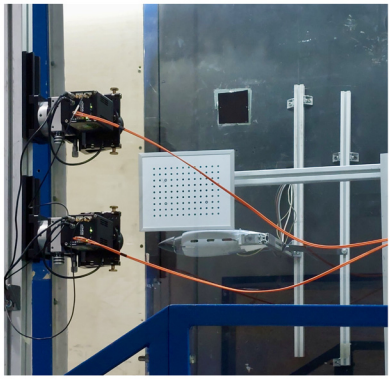

(b)Cameras set up

FIG. 3. PIV setup in the test section.

side-by-side tests. Therefore, only the lower propeller's performance will be discussed in the following. Figures 4 and 5 present the comparison of the averaged thrust coefficient (C_T) and power coefficient (C_P) measurements for the isolated propeller and for the lower propeller in the side-by-side configurations, covering all the lateral separation distances tested. A 95% simultaneous confidence band was calculated for each point based on these four load measurement repetitions and plotted as errorbars on the thrust and power coefficient curves' comparison.

In particular, to provide insight about the effects on aerodynamic performance related to the dual-propeller system with respect to a single propeller configuration in descent flight conditions, Figs. 4(a) and 5(a) show the comparison between the thrust and power coefficient curves measured for the single propeller configuration and for the lower SBS propeller at the maximum lateral distance tested, i.e., $D_y = 1R$.

By observing the thrust coefficient curve measured for the single propeller [see Fig. 4(a)], a loading drop appears at approximately $DR \approx 1$, which is consistent with the physical occurrence of VRS. As the descent ratio further increases, the propeller begins to recover some of its thrust. This behavior is in accordance with the known transition from VRS and turbulent-wake-state to windmill-brake or autorotation regimes, where the descent airflow becomes more stable.[1] A similar trend can be observed in the power coefficient curve [see Fig. 5(a)], as a distinct drop in C_P is also visible around $DR \approx 1$, corresponding to the VRS onset. However, unlike the thrust coefficient, the power coefficient further decreases as the descent ratio increases beyond this point. This progressive C_P reduction reflects the decreasing power demand of the rotor as it enters an energy-absorbing aerodynamic state. Comparing the isolated case and the side-by-side configuration with the maximum distance between the propellers, the former appears more severe in terms of thrust loss at VRS occurrence, although the latter shows a horizontal shift toward lower descent ratios. This suggests that, despite the significant relative distance between the two propellers, the presence of a second descending propeller has an apparent effect, leading to an earlier entry into the VRS condition, i.e., at a lower descent velocity compared to the single propeller configuration.

The shift in the observed descent ratio at the onset of the VRS in side-by-side configurations can be interpreted through an adaptation of momentum theory to interacting rotors flow fields. According to classical theory applied to a single rotor, VRS onset is typically expected when the descent velocity (V_∞) is of the same order as the

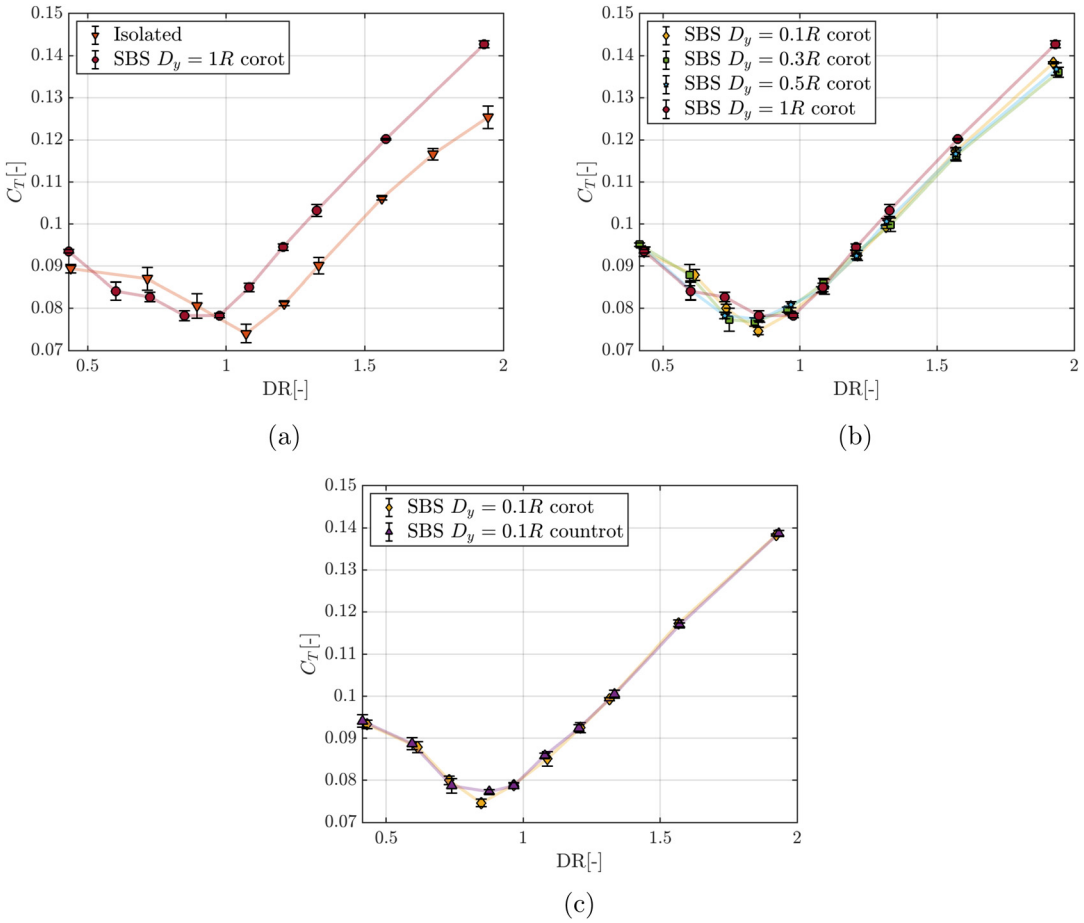

FIG. 4. Comparison of the thrust (C_T) coefficient measured for the lower propeller in the different configurations as function of the descent ratio (DR).

hover induced velocity (v_h). However, for interacting side-by-side neighbor rotors, the local flow environment is fundamentally altered by their mutual inflow alteration providing an increase in the induced velocity at the rotors plane and of the upward momentum flux produced by the dual propellers system. Thus, the condition for VRS onset is reached at a lower freestream velocity than in the single propeller case explaining the shift of the thrust drop observed from the side-by-side propellers measurements toward a lower descent ratio.

On the other hand, a mitigation of the VRS effects in terms of load loss amplitude at VRS onset is apparent due to the presence of the second propeller. These outcomes are in accordance with the experimental results obtained by Longobardo *et al.*[8] comparing the aerodynamic performance of a single rotor and a quad-rotor configuration under descent flight conditions and can be correlated with a wake entrainment effect provided by the mutual interaction of neighbor propellers, as will be discussed in detail analyzing the present PIV results.

The effect of the variation of the lateral distance on the lower SBS propeller performance can be evaluated from the load curve comparison shown in Figs. 4(b) and 5(b), where the load coefficient curves obtained for all the tested SBS configurations with co-rotating propellers are compared. As a matter of fact, the load coefficient curves exhibit slight variations with respect to the different lateral distance D_y, thus suggesting quite limited effects on the dual-propeller system, particularly regarding VRS onset, due to this geometrical parameter. A similar outcome can be deduced for the effect of the blade sense of rotation, as the load coefficient curves measured for the lower propeller in the SBS configuration at the same lateral distance $D_y = 0.1R$ but with co-rotating and counter-rotating blades show slightly different behavior [see Figs. 4(c) and 5(c)]. In particular, switching to the counter-rotating side-by-side configuration allows for a partial reduction of the thrust loss intensity at VRS onset. To provide a quantitative and more appreciable representation of the dual-propeller system effects on performance losses, Fig. 6 compares the percentage thrust drop experienced by the lower SBS propeller at the descent ratio corresponding to VRS onset with respect to the single propeller in hover condition. This analysis highlights how, in general, all side-by-side configurations are characterized by a lower loss of propeller thrust compared to the isolated propeller case, thus confirming the mitigation of the VRS effect on propeller performance due to the dual-propeller configuration. Moreover, this representation allows one to appreciate that increasing the distance between the propellers with the same sense of rotation, the thrust loss at VRS onset slightly decreases. This

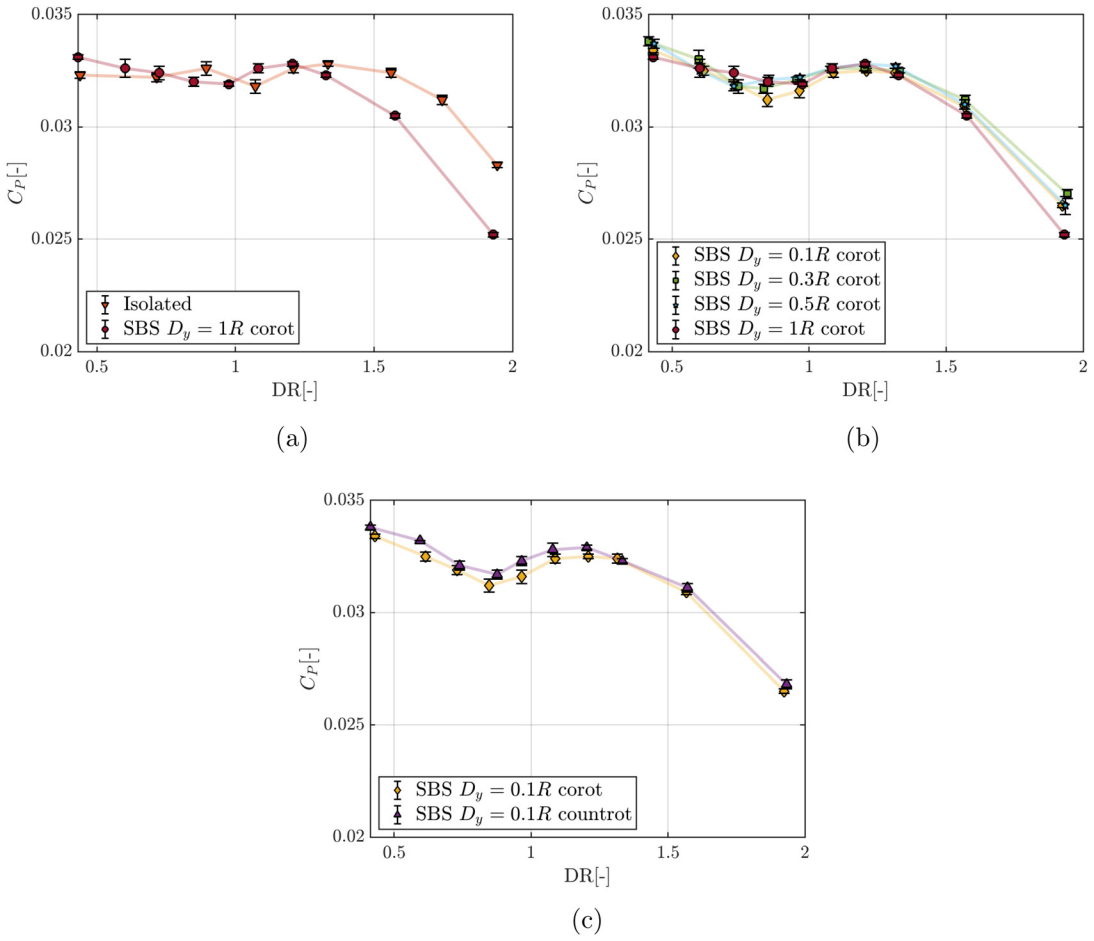

FIG. 5. Comparison of the power (C_P) coefficient measured for the lower propeller in the different configurations as function of the descent ratio (DR).

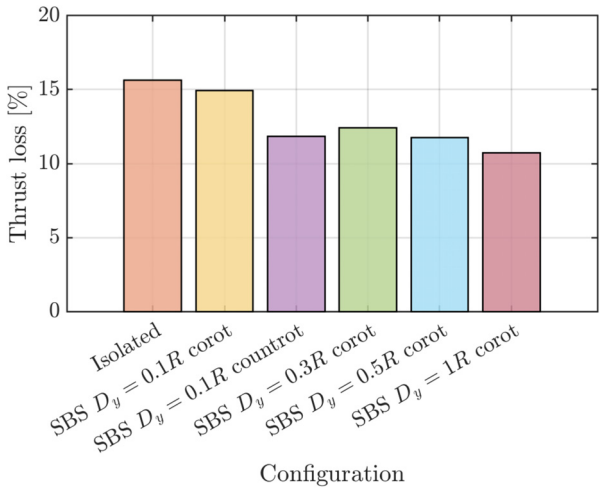

FIG. 6. Comparison of percentage thrust loss occurring at VRS descent ratio with respect to the isolated propeller in hover condition.

outcome suggests lowering the lateral distances increases the aerodynamic interaction between the propellers and the robustness of the VRS severity in terms of performance, thus introducing a slight increased detrimental effect from a safety margin perspective. Additionally, the comparison of the thrust loss between co-rotating and counter-rotating blade configurations at the same lowest lateral separation distance between the propellers ($D_y = 0.1R$) confirms a slight attenuation of the thrust loss for the latter configuration.

To gain further insight into the analysis of performance losses due to VRS occurrence, a normalized representation of the thrust coefficient with respect to the value measured in hover condition for the isolated propeller (C_{T_0}) is discussed. Indeed, when the normalized thrust coefficient C_T/C_{T_0} drops below unity, the propeller is generating less thrust than in the hover case. The extent of the region where this condition is encountered and the corresponding descent ratio range was considered a meaningful indicator of VRS severity for the different configurations. Although the area under the curve could serve as a global metric of thrust loss, it is important to highlight that this analysis could be limited by the relatively sparse experimental points available among the configurations tested. However, Fig. 7 illustrates an enlarged view of the normalized thrust coefficient curves over the descent ratio area where C_T/C_{T_0} is below unity. This analysis allows for a better appreciation of the operational descent ratio range in which thrust performance degradation occurs with respect to the hover condition for the different configurations.

It is evident that the single propeller configuration exhibits the widest thrust loss area with respect to the hover condition, showing the highest amplitudes of the thrust loss peak and the largest descent ratio range where the non-dimensional thrust coefficient is below unity [see Fig. 7(a)]. This representation indicates that the single propeller in descent flight is subjected to a higher performance degradation that occurs over a larger descent velocity range compared to the side-by-side configuration. This analysis supports the outcome that the side-by-side configuration attenuates the detrimental effects of VRS occurrence, both in terms of maximum thrust loss and the effectiveness of the degraded performance over the flight envelope.

In addition, an interesting qualitative trend emerges by analyzing the curves obtained for the lower SBS propeller at different lateral distances [see Fig. 7(b)]. Indeed, as the lateral distance between the two propellers decreases, the descent ratio range affected by thrust degradation becomes slightly smaller. Furthermore, the comparison of the curves between the SBS co-rotating and counter-rotating blade configurations at equal lowest lateral spacing indicates that the blades' rotational direction does not affect the descent ratio extent of propeller performance degradation with respect to hover, with the exception of an attenuated peak occurring at VRS onset for the counter-rotating configuration [see Fig. 7(c)].

B. Particle image velocimetry

PIV measurements were performed for all the single and dual-propeller configurations under investigation, at four different descent ratios. For each test configuration, the averaged PIV flow fields are shown in terms of contours of the in-plane velocity magnitude $|V|$ superimposed on in-plane streamlines.

The first analysis, whose results are shown in Fig. 8, focuses on the single propeller configuration, used as a reference to investigate the general behavior of the vortex ring without interference from a second propeller. As the descent speed increases, a recirculation region gradually arises from below the propeller disk, eventually organizing at $DR = 1.1$ into a clear vortex ring structure at the propeller disk altitude. This structure moves upstream as the descent ratio further increases, in agreement with the known progression of VRS generation.

Expanding the flow field analysis to side-by-side propeller configurations allows for the investigation of the dual-system installation effect on vortex ring generation. Figure 9 presents the flow fields obtained for a lateral distance of $D_y = 1R$, where the formation of two clearly separated vortex rings is apparent. The flow fields captured by PIV surveys for each of the two propellers resemble the VRS progression observed for the single one and reveal a quite symmetrical behavior, as no significant deformation of the vortical structures is observed. In particular, the two distinct vortex rings reach the propeller disks altitude at an earlier descent ratio, i.e., $DR = 0.9$, compared to the single propeller condition, thus confirming the earlier occurrence of VRS for the dual-propeller system observed from the load measurements. Figure 10 shows the flow fields corresponding to side-by-side propellers at $D_y = 0.5R$. As the distance between the propellers is reduced, the inner vortices begin to interact. Despite evident deformation and compression, two distinct vortex structures remain clearly detectable, although with a visibly reduced core radius. As the descent ratio increases, the evolution of the vortex structures follows the behavior previously observed, characterized by displacement from the propeller disk plane and radial expansion, ultimately leading to dissipation.

A further reduction in the inter-rotor lateral spacing leads to enhanced vortex ring interaction, deformation, and eventual merging. At $D_y = 0.3R$, as shown by the flow fields in Fig. 11, the characteristic dual-vortex structure between the propellers is no longer observed at $DR = 0.9$. This phenomenon becomes more pronounced at $D_y = 0.1R$, as illustrated in Fig. 12, where the lack of vortical structures in the region between the two propellers suggests the formation of a single, unified vortex ring enclosing both rotors. As a matter of fact, the proximity of the two propellers leads to wake entrainment, where the individual slipstreams begin to merge into a single, broader

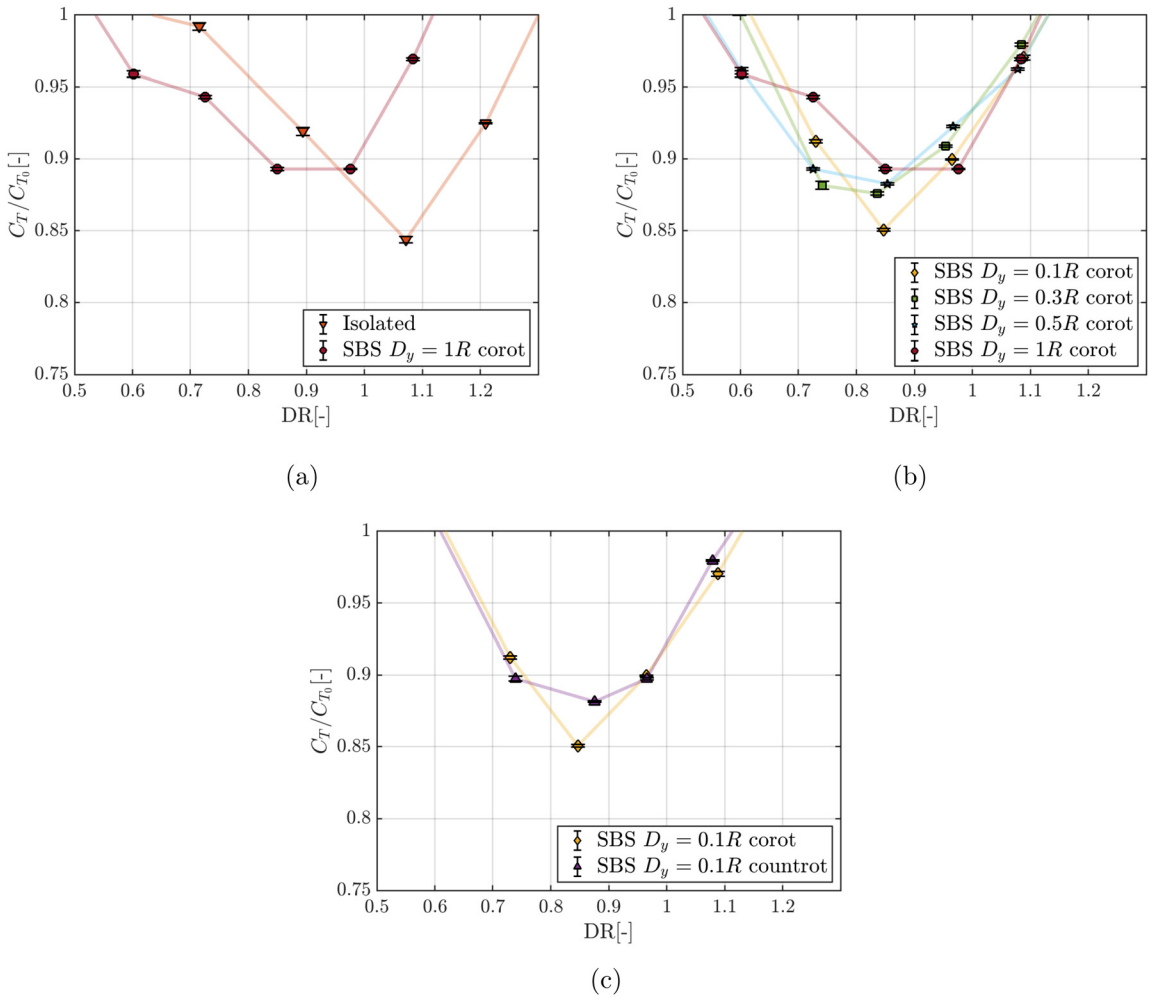

FIG. 7. Comparison of the normalized thrust coefficient (C_T) with respect to the value measured for the single propeller in hover (C_{T_0}) for the different configurations as a function of the descent ratio (DR).

wake. This wake entrainment effectively increases the capture area of the vortex system causing the dual-propellers to behave as a modified single rotor disk characterized by a larger effective area. Thus, also the recirculation effects of the unified vortex ring are attenuated as spread over a larger effective area, explaining the less severe local peak loading loss observed for the dual-propeller system with respect to single propeller case. The delocalization and redistribution of vortical strength over a larger effective disk area are also responsible of the smoother thrust and power drop behavior observed for the dual-propellers system. Indeed, the flow recirculation for the unified vortex structure is stretched around the global perimeter of the system preventing the vortex ring from reaching the same level of concentrated coherence seen in the single propeller case.

Interestingly, once the VRS condition is exceeded as the descent ratio increases, two separate and independent vortical structures progressively reappear, each one detaching from the corresponding propeller disk plane and propagating downstream. It can be observed that the formation of inner vortices and the consequent breakdown of the single, unified vortex ring generated by both propellers occur at progressively higher descent ratios as the distance between the propellers decreases.

The analysis of the counter-rotating configuration, presented in Fig. 13, indicates that even when maintaining the lowest lateral distance between the propellers ($D_y = 0.1R$) but with opposite sense of rotation, the overall flow field topology remains fundamentally unaltered. This observation suggests that the sense of rotation has a negligible effect on the overall flow characteristics and on the large-scale vortex structure, which is in accordance with the slight discrepancies encountered when comparing the load coefficient curves shown in Figs. 4(c) and 5(c).

Finally, Fig. 14 provides immediate insight into the interactional effects between the two propellers on the evolution of the vortex structures as their lateral distance is reduced. In particular, this snapshot is provided at the descent ratio corresponding to the flight condition closest to VRS occurrence for all configurations, i.e., $DR = 0.9$. As a matter of fact, the lateral distance $D_y = 1R$ is sufficient to allow the

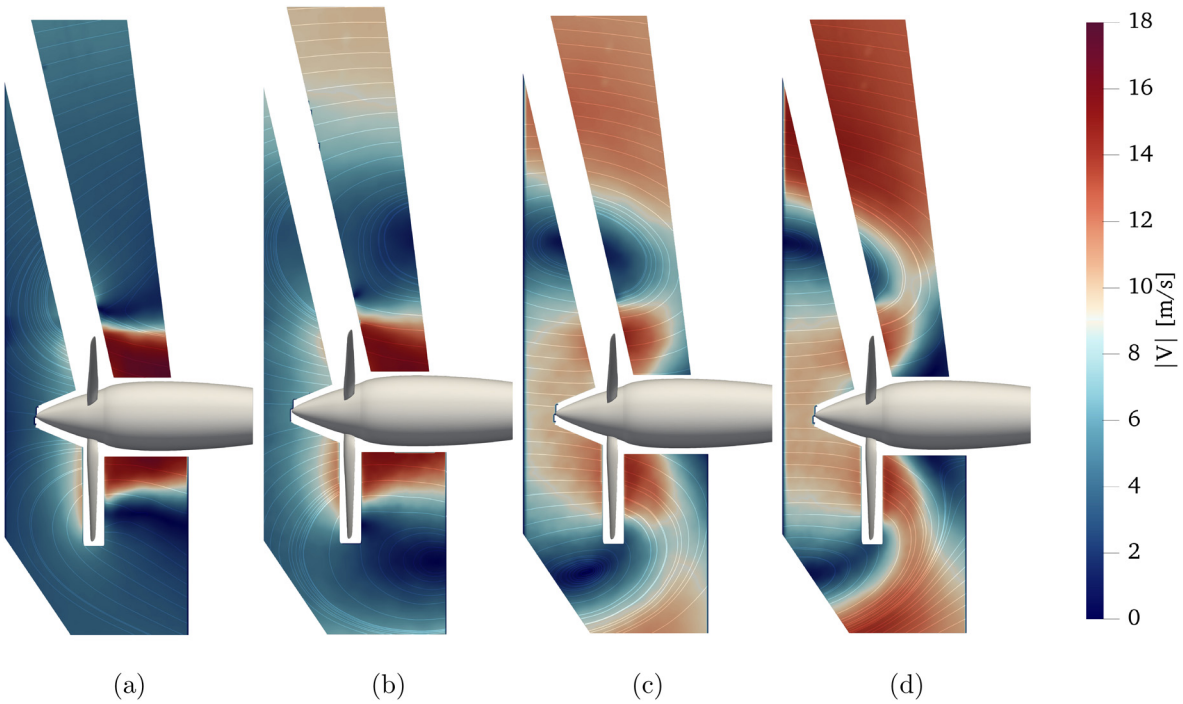

FIG. 8. Comparison of the PIV averaged flow fields for single propeller configuration, (a) $DR = 0.5$, (b) $DR = 0.9$, (c) $DR = 1.1$, and (d) $DR = 1.3$.

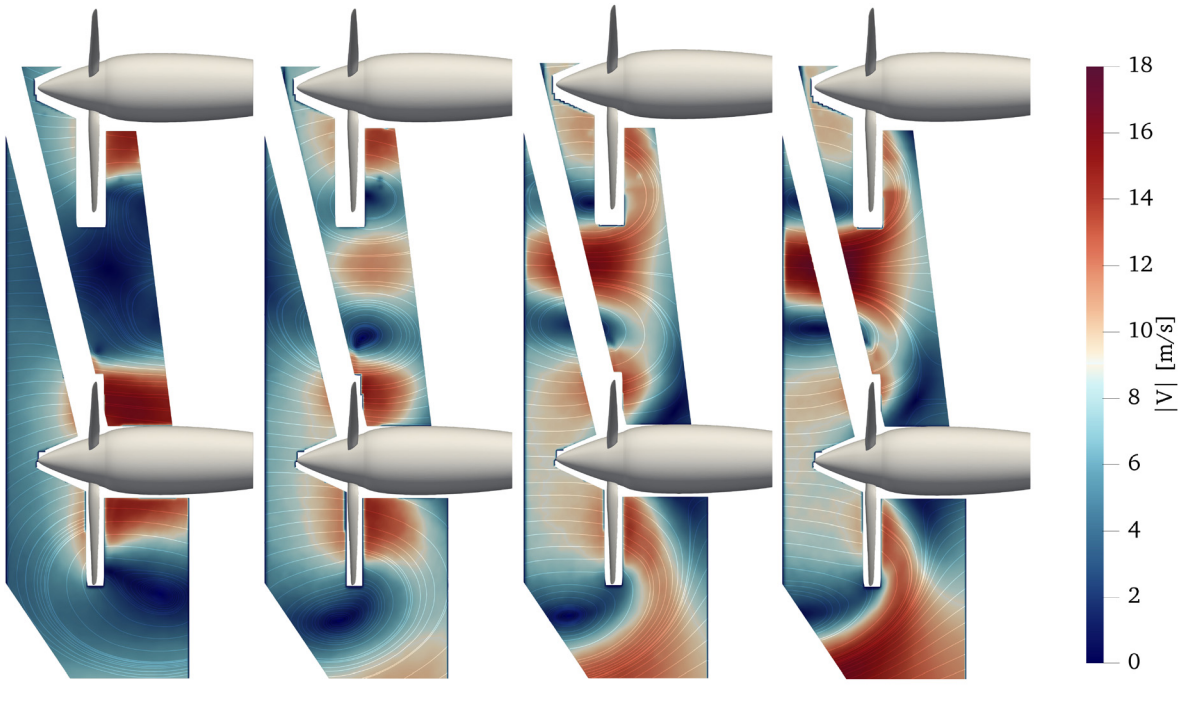

FIG. 9. Comparison of the PIV averaged flow fields for side-by-side co-rotating propellers configuration with $D_y = 1R$, (a) $DR = 0.7$, (b) $DR = 0.9$, (c) $DR = 1.1$, and (d) $DR = 1.3$.

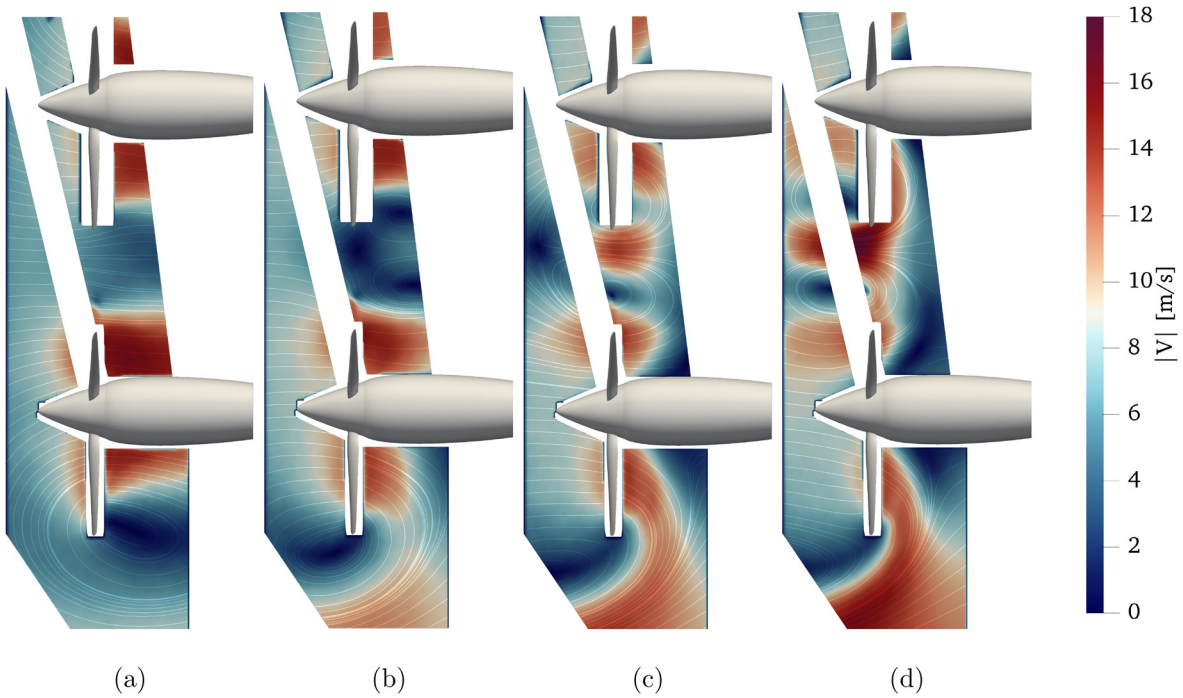

FIG. 10. Comparison of the PIV averaged flow fields for side-by-side co-rotating propeller configuration with $D_y = 0.5$R, (a) $DR = 0.7$, (b) $DR = 0.9$, (c) $DR = 1.1$, and (d) $DR = 1.3$.

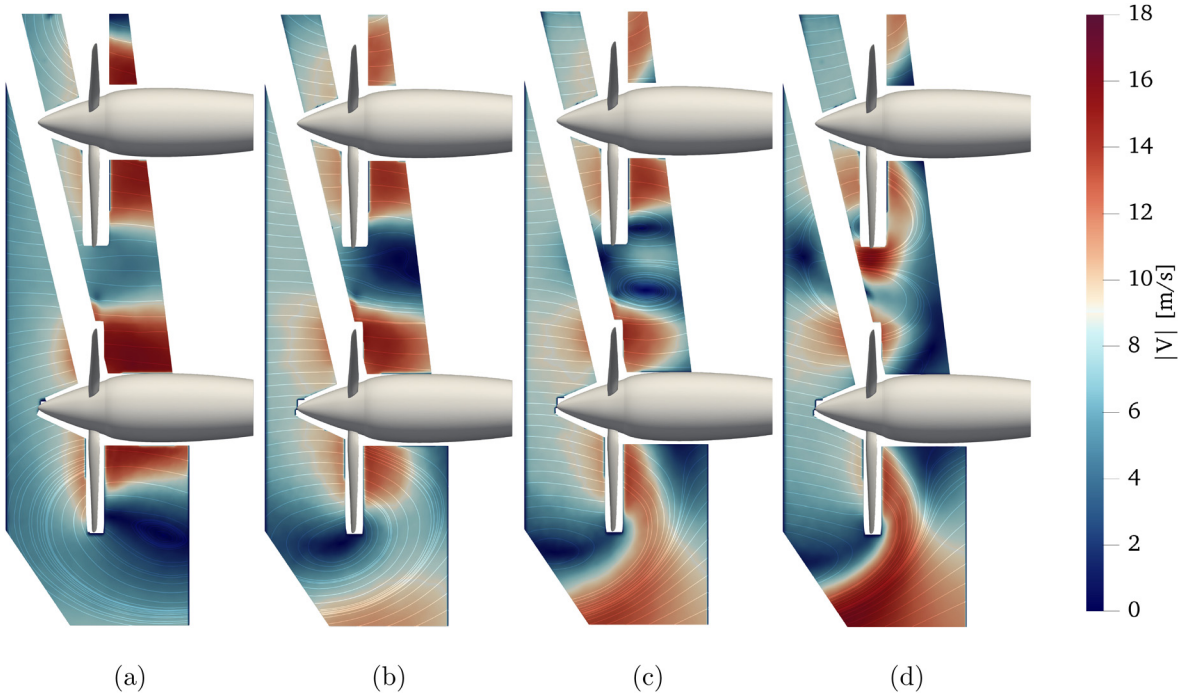

FIG. 11. Comparison of the PIV averaged flow fields for side-by-side co-rotating propeller configuration with $D_y = 0.3$R, (a) $DR = 0.7$, (b) $DR = 0.9$, (c) $DR = 1.1$, and (d) $DR = 1.3$.

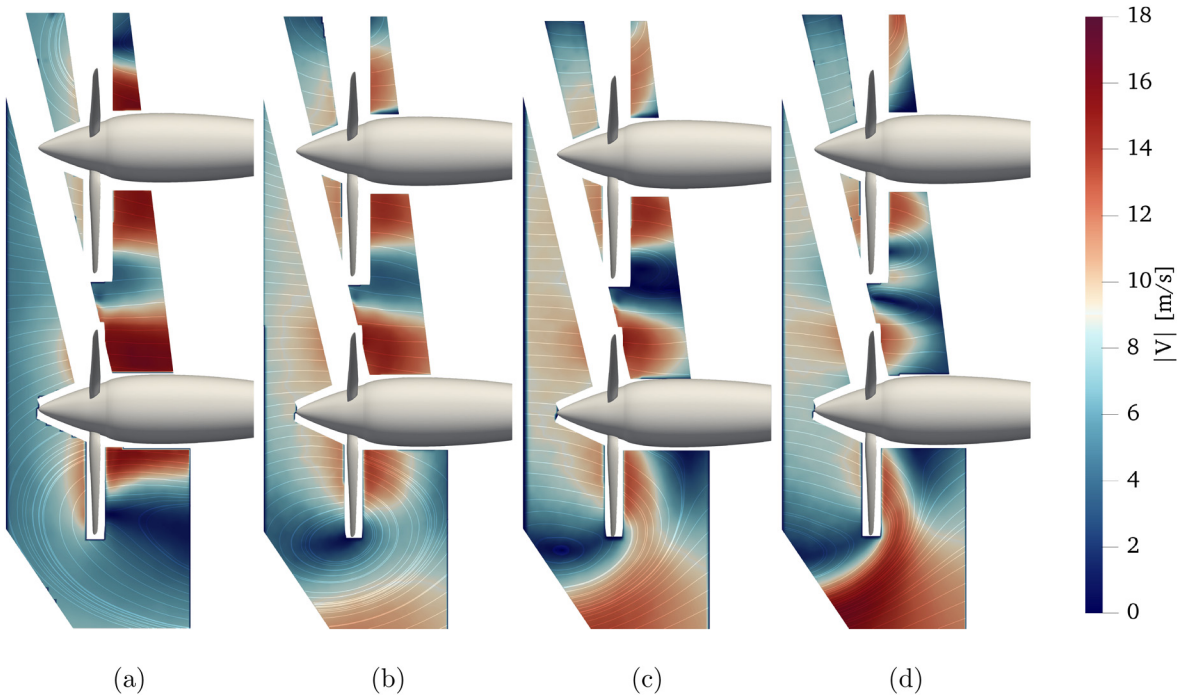

FIG. 12. Comparison of the PIV averaged flow fields for side-by-side co-rotating propeller configuration with $D_y = 0.1$R, (a) $DR = 0.7$, (b) $DR = 0.9$, (c) $DR = 1.1$, and (d) $DR = 1.3$.

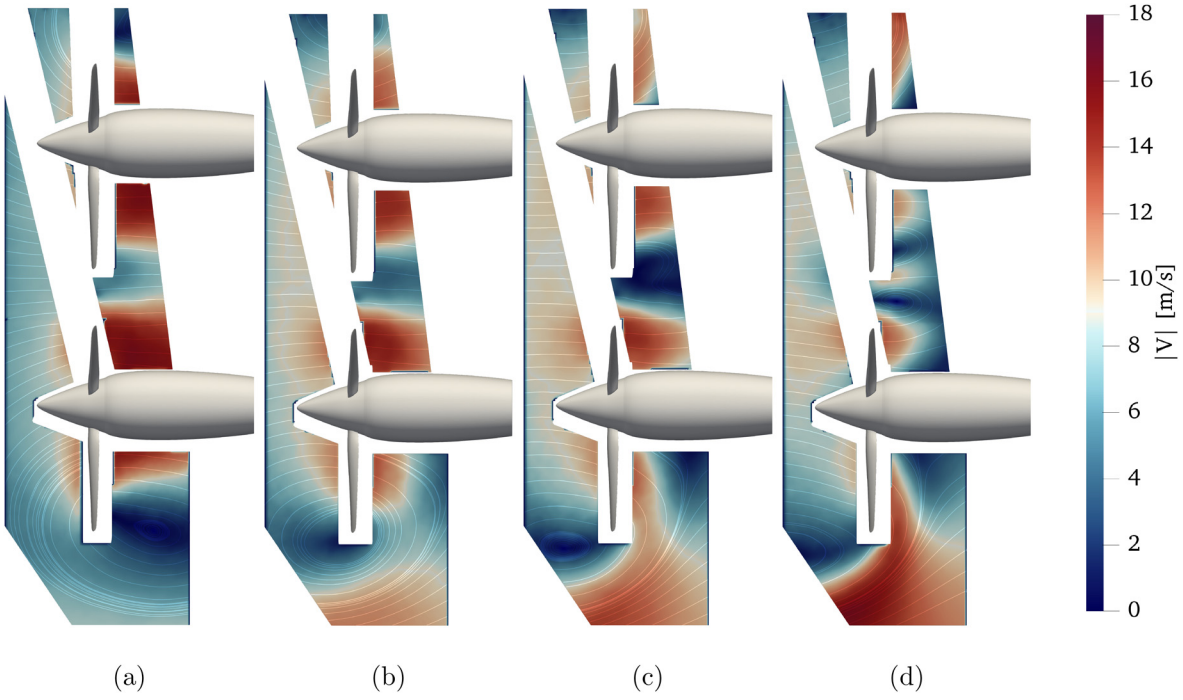

FIG. 13. Comparison of the PIV averaged flow fields for side-by-side counter-rotating propeller configuration with $D_y = 0.1$R, (a) $DR = 0.7$, (b) $DR = 0.9$, (c) $DR = 1.1$, and (d) $DR = 1.3$.

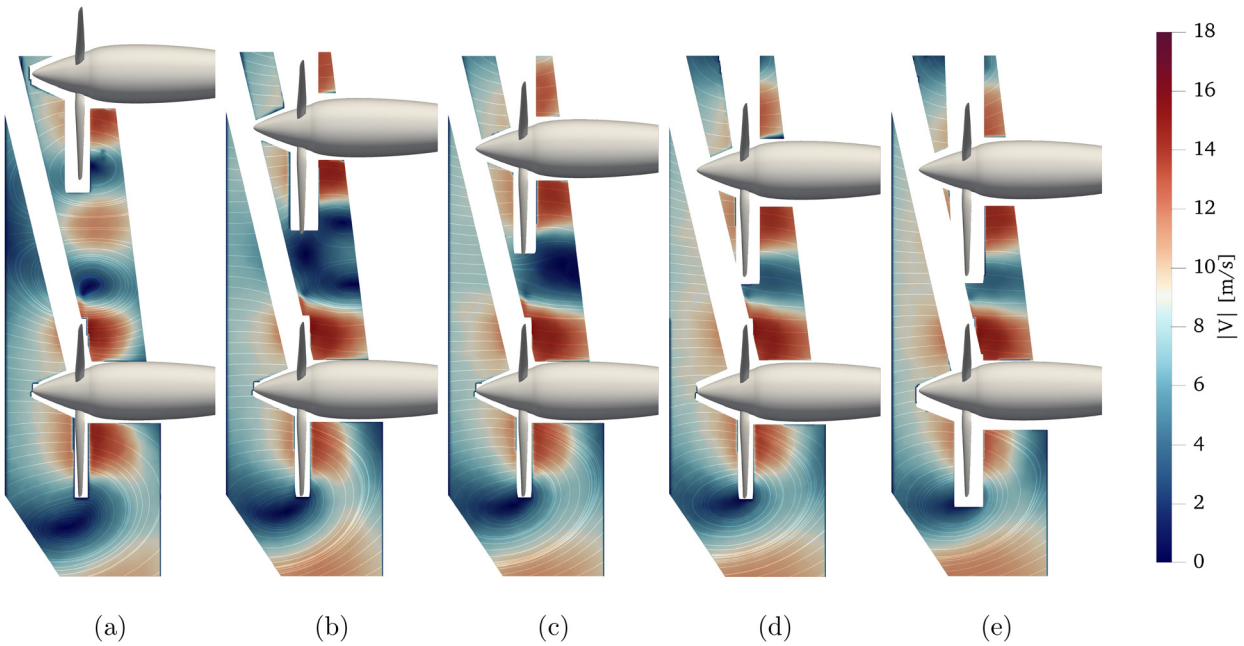

FIG. 14. Comparison of the PIV averaged flow fields for side-by-side propeller configuration at $DR = 0.9$, (a) $D_y = 1$R, (b) $D_y = 0.5$R, (c) $D_y = 0.3$R, (d) $D_y = 0.1$R, and (e) $D_y = 0.1$R counter-rotating.

generation of two distinct vortex rings, thus suggesting negligible interaction effects between the two propellers, which effectively act as single, separated propellers. Interactional effects become relevant by halving the distance between the propellers, as at $D_y = 0.5R$, the inner vortices already appear compressed and reduced in size, while still maintaining a distinct structure and coherence. Further reduction of lateral spacing increases the effects of the interactional mechanisms, leading to the progressive coalescence of the inner vortices, culminating in a complete merging at $D_y = 0.1R$.

In order to further investigate the aerodynamic phenomena observed through flow field measurements, a quantitative analysis was conducted regarding dimension and intensity of the vortical structures generated at the onset of VRS in the different configurations (i.e., DR = 1.1 for the isolated propeller and DR = 0.9 for side-by-side configurations), in particular, focusing on the outer vortex exposed by PIV data around the lower propeller. With this aim, the vortex characteristics were evaluated on the base of the analysis of the in-plane streamlines obtained from the two-dimensional PIV-averaged flow fields. Indeed, when streamlines twist or close around a circular structure, they provide a clear identification of the vortex core. In particular, according to the methodology described by Ari Sadarjoen and Post,[21] in vortical regions of the flow field, the centers of curvature of several nearly circular streamlines accumulate at a point, that is considered the vortex center position. As done in the work by Savino *et al.*,[12] this method was applied to the present PIV flow field to identify the core center of the vortex shape generated in the outer flow region around the lower propeller. The vortex core radius (R_v) was determined computing the tangential velocity within this flow field are and identifying the radial distance between the vortex center and the point where the tangential velocity component reaches its maximum value ($V_{\theta_{max}}$), as done in Gibertini *et al.*[22] Those two latter values were, therefore, used to calculate the circulation (Γ) considered as an indicator of the vortex intensity. Table II compares the radius and circulation calculated from PIV data for the outer vortex generated around the lower propeller in all the tested configurations at VRS onset.

The highest values of both the vortex radius and the circulation are observed in the isolated propeller case, while the introduction of a side-by-side propeller configuration results, as expected from the previous loads and flow fields analysis, in a reduction of both quantities. In particular, for co-rotating propellers as the lateral spacing increases, the vortex size and intensity progressively increase, approaching the values of the isolated configuration for the $D_y = 1R$ condition. These results are coherent with the previous observations, as a reduction in the distance between the two propellers causes a progressive wake entrainment, which leads to a reduction in the loads seen by the

TABLE II. Comparison of the radius and circulation calculated from PIV data for the lower propeller outer vortex in the different tested configurations at VRS onset, i.e., DR = 1.1 for the isolated propeller and DR = 0.9 for side-by-side propellers configurations.

Configuration	$R_v/R\,(-)$	$\Gamma/(V_\infty R)\,(-)$
Isolated	0.78	5.38
SBS 0.1R co-rotating	0.54	3.53
SBS 0.1R counter-rotating	0.59	4.40
SBS 0.3R co-rotating	0.62	4.15
SBS 0.5R co-rotating	0.65	4.73
SBS 1R co-rotating	0.74	5.56

propeller disk and a decrease in the dimension and intensity of the outer vortex. At the minimum lateral spacing, counter-rotating propellers exhibit slightly higher vortex radius and circulation values compared to the co-rotating configuration at the same D_y, confirming that an opposite sense of rotation partially alleviates proximity effects by weakening wake merging. In addition, the slight variations between the vortex circulations calculated in the whole range of lateral distance tested justify the small percentage differences of thrust deficit observed for the lower propeller in all the investigated test cases (see Fig. 6).

IV. CONCLUSIONS

A comprehensive experimental campaign was performed to investigate the Vortex Ring State (VRS) for side-by-side propeller configurations in descent flight conditions. Wind tunnel tests enabled a re-evaluation of the VRS phenomenon by considering the effects of aerodynamic interactions and multi-propeller installation, which are typical of eVTOL aircraft configurations. In particular, a novel aspect of this activity was the ability to estimate the effect of varying the lateral distance between the propellers on both propeller performance and the flow physics related to the generation of the vortex ring structure.

Measurements of aerodynamic load coefficients showed that the installation of the second side-by-side propeller causes the onset of VRS at an earlier descent ratio compared to a single propeller configuration. Indeed, the VRS onset for a dual-propeller system occurs with a descent ratio variation of about 0.2 with respect to the single propeller case. The observed feature is related to the mutual inflow alteration of the dual-propeller system providing an increase in the induced velocity at the rotors plane. This outcome represents an important indication for eVTOL flight scenarios, suggesting that multi-propeller architectures could experience a robust drop in aerodynamic performance at an earlier descent speed compared to classical helicopter configurations. On the other hand, load measurements also indicate that for side-by-side propellers, the VRS onset is characterized by a smoother drop in thrust and power coefficients compared to the single propeller configuration. Indeed, for the dual-propeller system at the higher lateral distance tested, i.e., $D_y = 1R$, loads measurements showed largest reduction of the percentage peak thrust loss at VRS onset of about 5% with respect to single propeller case. This loading attenuation is related to wake entrainment occurring in the dual-propeller system providing an increase in the effective capture area of the vortex system. Additionally, the attenuation of the VRS detrimental effects related to the dual-propeller installation is supported by the smaller area exposed by the thrust coefficient curves below the reference performance of the single propeller in hover. This outcome indicates a less severe effect of VRS on multi-propeller aircraft lifting capabilities and also occurs over a slightly more limited range of descent speed. Further novel findings from the present load measurements are related to the fact that the variation of the lateral distance and the blades' sense of rotation do not significantly change the performance drop observed at VRS onset, as a maximum variation of only a few percent of the thrust experienced by the single propeller in hover can be appreciated across the entire range of tested conditions.

PIV surveys enabled a full characterization of the flow physics related to the VRS phenomenon, particularly highlighting the differences in vortex ring generation due to the second propeller installation and the aerodynamic interaction mechanisms occurring when varying the lateral distance between propellers. First, the comparison of the flow fields confirms the load measurement outcomes by showing the generation of the large vortex ring structure typical of VRS in the region of the propeller disk at an earlier descent ratio for the side-by-side configurations compared to the single propeller one. Moreover, while at the highest lateral distance tested, each of the two side-by-side propellers exhibits the classical formation of the vortex ring structure around the blade area, diminishing the tip-to-tip lateral distance between the side-by-side propellers leads to the interaction of the inner vortical structures, which reduce their dimensions until they coalesce. This suggests the generation of a unique vortex ring structure wrapping the dual-propeller system. Considering the different side-by-side configurations at the VRS onset, the progressive development of the wake entrainment is also reflected in the evolution of the outer vortex radius and circulation. Both quantities increase with the relative spacing, approaching values comparable to the isolated propeller case at the maximum lateral distance.

Generally, the main achievement of the present activity was to contribute to the guidelines to be considered in the preliminary design of multi-propeller architectures by providing quantitative indications related to the performance variation due to the typical installation effects occurring in eVTOL aircraft architectures. Moreover, the comprehensive experimental database obtained over a free propeller geometry can be considered a robust benchmark for the validation of multi-fidelity numerical solvers tackling this complex aerodynamics problem, as will be done in the framework of the new Action Group supported by GARTEUR.

ACKNOWLEDGMENTS

The research leading to the presented results has been addressed within the framework of the RC/AG-28 "eVTOL aircraft Vortex-Ring-State investigations," supported by GARTEUR. Authors would like to acknowledge Caterina Saglio, Donato Grassi, and Luca Riccobene for their support during the wind tunnel tests.

AUTHOR DECLARATIONS

Conflict of Interest

The authors have no conflicts to disclose.

Author Contributions

G. Bucherelli: Conceptualization (equal); Data curation (equal); Formal analysis (equal); Investigation (equal); Methodology (equal); Software (equal); Validation (equal); Visualization (equal); Writing – original draft (equal). **D. Granata:** Conceptualization (equal); Data curation (equal); Formal analysis (equal); Investigation (equal); Methodology (supporting); Software (equal); Validation (equal); Visualization (supporting). **A. Savino:** Conceptualization (equal); Data curation (supporting); Formal analysis (supporting); Investigation (equal); Methodology (equal); Project administration (supporting); Software (supporting); Supervision (supporting); Writing – review & editing (equal). **A. Zanotti:** Conceptualization (equal); Formal analysis (equal); Funding acquisition (equal); Methodology (equal); Project administration (equal); Supervision (equal); Writing – original draft (equal); Writing – review & editing (equal).

DATA AVAILABILITY

The data that support the findings of this study are available from the corresponding author upon reasonable request.

NOMENCLATURE

C_P	Power coefficient $= P/(\rho D^5 n^3)$ (-)
C_T	Thrust coefficient $= T/(\rho D^4 n^2)$ (-)
C_{T_0}	Thrust coefficient in hover (-)
D	Propeller diameter (m)
D_y	Tip-to-tip lateral distance between propellers (m)
DR	Descent ratio $= V_\infty / v_h$
n	Rotational speed (rev s^{-1})
P	Propeller power (W)
R	Propeller radius (m)
R_v	Vortex radius (m)
Re_c	Reynolds number based on blade chord at 75% radius
T	Propeller thrust (N)
T_h	Single propeller thrust in hover (N)
$V_{\theta_{\max}}$	Maximum tangential velocity component (m s^{-1})
V_∞	Freestream velocity magnitude (m s^{-1})
$\lvert V \rvert$	In-plane velocity magnitude (m s^{-1})
v_h	Single propeller induced velocity $= \sqrt{T_h/(2\rho\pi R^2)}$
$v_{\theta_{\max}}$	Tangential velocity at R_{vor}
Γ	Vortex circulation $= 2\pi R_v V_{\theta_{\max}}$ (m^2 s^{-1})
θ	Blade pitch angle at 75% radius (°)
ρ	Freestream air density (kg m^{-3})

REFERENCES

[1]G. J. Leishman, *Principles of Helicopter Aerodynamics* (Cambridge University Press, 2006).
[2]M. Veismann, D. Yos, and M. Gharib, "Parametric study of small-scale rotors in axial descent," Phys. Fluids **34**, 035124 (2022).
[3]W. Johnson, *Rotorcraft Aeromechanics*, Cambridge Aerospace Series (Cambridge University Press, Cambridge, 2013).
[4]M. D. Betzina, "Tiltrotor descent aerodynamics: A small-scale experimental investigation of vortex ring state," in American Helicopter Society 57th Annual Forum, Washington, DC, 2001.
[5]A. Brand, R. Kisor, R. Blyth, D. Mason, and C. Host, "V-22 high rate of descent (HROD) test procedures and long record analysis," in American Helicopter Society 60th Annual Forum, Baltimore, MD, 2004.
[6]O. Shetty and M. Selig, "Small-scale propellers operating in the vortex ring state," AIAA Paper No. 2011-1254, 2011.
[7]J. Stack, "Experimental investigation of rotor vortex wakes in descent," AIAA Paper No. 2004-297, 2004.
[8]G. Longobardo, A. Heintz, J. Braukmann, C. Wolf, J. Raddatz, T. Astarita, F. De Gregorio, A. Gardner, and M. Raffel, "Experimental investigation of vortex ring state for multicopters," in Proceedings of the 51st European Rotorcraft Forum, Venice, Italy, 9–12 September (2025).
[9]R. E. Brown, "Are eVTOL aircraft inherently more susceptible to the vortex ring state than conventional helicopters?," in Proceedings of the 48th European Rotorcraft Forum, 2022.
[10]T. Jeong, Y. Hong, and K. Yee, "Extension of the analytic vortex ring state model for eVTOL application," in *80th Annual Vertical Flight Society Forum and Technology Display, FORUM 2024* (Vertical Flight Society, 2024).
[11]D. J. Pickles, D. Zagaglia, A. Busse, and R. B. Green, "Vortex ring state of a shrouded rotor: An experimental survey," Exp. Fluids **64**, 116 (2023).
[12]A. Savino, A. Gianotti, G. Droandi, M. Kerho, and A. Zanotti, "Experimental investigation of vortex ring state in an eVTOL propeller," Aerosp. Sci. Technol. **165**, 110475 (2025).
[13]A. Savino, A. Gianotti, G. Droandi, M. Kerho, and A. Zanotti, "Experimental investigation of vortex ring state conditions for archer maker eVTOL tilter propeller," in Vertical Flight Society 81st Annual Forum and Technology Display, 2025.
[14]D. Zagaglia *et al.*, "Experimental investigation into the vortex ring state of multi-rotor configurations," in 50th European Rotorcraft Forum, 2024.
[15]D. Granata, A. Savino, D. Grassi, L. Riccobene, and A. Zanotti, "Aerodynamic and aeroacoustics investigation of tandem propellers in hover for eVTOL configurations," Aerosp. Sci. Technol. **155**, 109740 (2024).
[16]A. Zanotti and D. Algarotti, "Aerodynamic interaction between tandem overlapping propellers in evtol airplane mode flight condition," Aerosp. Sci. Technol. **124**, 107518 (2022).
[17]A. Zanotti, A. Velo, C. Pepe, A. Savino, D. Grassi, and L. Riccobene, "Aerodynamic interaction between tandem propellers in eVTOL transition flight configurations," Aerosp. Sci. Technol. **147**, 109017 (2024).
[18]P. GmbH, see https://www.pivtec.com/ for "Pivview 2c, version 3.9.3" (2023).
[19]M. Raffel, C. Willert, S. Wereley, and J. Kompenhans, *Particle Image Velocimetry—A Practical Guide* (Springer, Berlin, 2007).
[20]F. De Gregorio, K. Pengel, and K. K, "A comprehensive PIV measurement campaign on a fully equipped helicopter model," Exp. Fluids **53**, 37–49 (2012).
[21]I. Ari Sadarjoen and F. H. Post, "Detection, quantification, and tracking of vortices using streamline geometry," Comput. Graphics **24**, 333–341 (2000).
[22]G. Gibertini, A. Mencarelli, and A. Zanotti, "Oscillating aerofoil and perpendicular vortex interaction," Proc. Inst. Mech. Eng., Part G **228**, 846–858 (2014).